

Implications for constrained supersymmetry of combined H.E.S.S. observations of dwarf galaxies, the Galactic halo and the Galactic Centre

Joachim Ripken¹, Jan Conrad¹, and Pat Scott²

¹Oskar Klein Centre for Cosmoparticle Physics and Department of Physics, Stockholm University, AlbaNova University Centre, SE-10691 Stockholm, Sweden

²Department of Physics, McGill University, 3600 rue University, Montréal, QC, H3A 2T8, Canada

Abstract

In order to place limits on dark matter (DM) properties using γ -ray observations, previous analyses have often assumed a very simple parametrisation of the γ -ray annihilation yield; typically, it has been assumed that annihilation proceeds through a single channel only. In realistic DM models, annihilation may occur into many different final states, making this quite a rough ansatz. With additional processes like virtual internal bremsstrahlung and final state radiation, this ansatz becomes even more incorrect, and the need for scans of explicit model parameter spaces becomes clear. Here we present scans of the parameter space of the Constrained Minimal Supersymmetric Standard Model (CMSSM), considering γ -ray spectra from three dwarf galaxies, the Galactic Centre region and the broader Galactic halo, as obtained with the High-Energy Stereoscopic System (H.E.S.S.). We present a series of likelihood scans combining the H.E.S.S. data with other experimental results. We show that observations of the Sagittarius, Carina and Sculptor dwarf galaxies disfavour the coannihilation region of the CMSSM and models with large annihilation cross-sections. This is true even under reasonable assumptions about the DM density profiles, and constitutes the strongest constraint to date on coannihilation models within the CMSSM. The Galactic halo has a similar, but weaker, effect. The Galactic Centre search is complicated by a strong (unknown) γ -ray source, and we see no effect on the CMSSM parameter space when assuming a realistic Galactic Centre DM density profile.

1 Introduction

The nature of the dark matter (DM) is still unclear, because its existence is so far only evident via its gravitational interaction with normal matter.

There are many possible ways to find DM, other than through its gravitational interactions. Direct detection experiments try to observe nuclear recoils from weak interactions with DM particles. Accelerator experiments search for hints of physics beyond the *standard model* (SM) of particle physics, which may provide clues as to the identity of dark matter. Indirect detection experiments try to identify secondary products of DM annihilation or decay, such as photons, neutrinos and anti-particles. Experiments typically search for characteristic spectral signatures of DM in the cosmic fluxes of such particles, allowing them to (hopefully) differentiate the DM signal from the myriad of astrophysical backgrounds they face.

There are many candidates for DM in extensions of the SM. The most popular is the neutralino, a linear combination of the superpartners of the neutral Higgs and electroweak gauge bosons seen in supersymmetric (SUSY) extensions of the SM. If R -parity is conserved, and the lightest neutralino is also the lightest supersymmetric particle (LSP), it can – depending on the underlying SUSY model parameters – deliver a relic density in the favoured range $0.094 \leq \Omega h^2 \leq 0.129$. Neutralinos are also Majorana particles, so would self-annihilate. If SUSY is to constitute a valid solution to the well-known *hierarchy problem* of the SM, it must be broken at ~ 1 TeV, giving sparticles such as the lightest neutralino masses of between ~ 10 GeV and ~ 10 TeV.

In the annihilation process, very high energy (VHE) γ -ray photons are produced with energies up to the neutralino mass. The emissivity of annihilating DM is proportional to ρ^2 , the square of the DM density. It is thus useful to search for VHE γ -radiation from regions where a high density of DM is expected. One such region is the centre of our own galaxy, the Galactic Centre (GC).

Limits on DM annihilation are generally based on assumptions about the form of the annihilation spectrum, ignoring the individual spectra of actual SUSY (or any other) models. This was perhaps reasonable until it was found that internal bremsstrahlung (IB), consisting of both final-state radiation (FSR) and virtual IB (VIB), can make large contributions to the photon spectrum [1]. In this case, gamma-ray spectra from different supersymmetric models can be very different, even when the neutralino mass is kept fixed. With this new development, it is necessary to compare the observed and predicted energy spectra from annihilation processes on an individual, model-by-model basis. This was first performed in a full SUSY scan using *Fermi*-LAT data on the dwarf galaxy Segue 1 [2].

The GC region has also been observed by the High Energy Stereoscopic System (H.E.S.S.), and high-energy gamma radiation has been detected [3, 4]. Because the observations seem to be incompatible with the total observed flux coming exclusively from neutralino annihilation, the hypotheses that DM annihilation makes a subdominant contribution has been investigated, resulting in limits on the DM self-annihilation cross-section [5, 6].

In this article we show the results of two full model scans in the parameter space of the Constrained Minimal Supersymmetric SM (CMSSM), comparing model predictions with H.E.S.S. data from the Sagittarius (SgrD), Carina and Sculptor dwarf galaxies, as well as the Galactic halo and Galactic Centre. First we show a simple random scan, producing

a set of CMSSM models compatible with constraints on the relic density and accelerator bounds included in DarkSUSY 5.0.4 [7, 8]. Later we show more advanced statistical scans, using the SuperBayeS package [9, 10, 11, 12, 13, 14, 15].

In section 2 we introduce the H.E.S.S. experiment and the data that we use for this work. Section 3 is about the theoretical framework of supersymmetric DM, and Section 4 describes our analysis of the H.E.S.S. data. Section 5 gives our results for the random scan using a spectrum from the GC source. Section 6 introduces the CMSSM parameter scan with SuperBayeS, considering the same GC spectrum. Section 7 describes a SuperBayeS scan taking into account the H.E.S.S. observations on the SgrD, whilst Secs. 8 and 9 introduce further constraints from the Carina and Sculptor dwarfs, and the Galactic halo, respectively. Section 10 finishes with a summary and outlook.

2 The H.E.S.S. telescope and data

H.E.S.S. is a system of 4 imaging atmospheric Čerenkov telescopes located in the Khomas highlands of Namibia, 120 km south west of Windhoek, and 1800 m above sea level. It is a γ -ray observatory sensitive to photons with energies between around 100 GeV and 100 TeV. The energy resolution is better than 15%. The angular resolution is better than 0.1° per event. [16]

The observed γ -ray spectrum for our scans including the GC data is from [4]. It contains 92.9 h of observations in the years 2004, 2005 and 2006. For the following analysis we employed the spectral points seen in the left-hand subfigure of Figure 2 in [4]. These data were already deconvolved from the instrumental response at the time of publication (see Ref. [4] for details), removing any need for us to convolve our predicted CMSSM spectra with the H.E.S.S. response.

H.E.S.S. observed the SgrD in June 2006 for ~ 12 h. No significant γ -ray excess was found and a flux upper limit of $\Phi(E > 250 \text{ GeV}) = 3.6 \cdot 10^{-12} \text{ cm}^{-2} \text{ s}^{-1}$ (95% CL) was calculated. Using these observations, and assuming a generic annihilation spectrum as well as two different DM density profiles, upper limits on the annihilation cross section $\langle \sigma v \rangle$ as function of the neutralino mass m_χ were calculated [17].

Observations of the Carina and Sculptor dwarf galaxies took place between January 2008 and December 2009 with ~ 15 h on Carina and ~ 12 h on Sculptor. Also here no significant γ -ray excess was found leading also to upper limits on the annihilation cross section as function of the neutralino mass [18].

Observations of the region around the GC were also used to search for diffuse γ -radiation originating from DM annihilation in the galactic halo. This radiation has not been found, so that again upper limits were calculated [19].

3 Theoretical framework

Adding the minimal additional particle content required to supersymmetrise the SM, along with the most general ‘soft’ SUSY-breaking Lagrangian terms (required to break but retain SUSY as a solution of the hierarchy problem), one arrives at the Minimal Supersymmetric Standard Model (MSSM). The addition of the soft terms introduces over 100 new parameters to the model, so even in the MSSM, simplifying assumptions are required in order to make any meaningful estimates of the parameters of the model. One way to arrive at such a simplified version of the model is to choose a specific breaking scheme, with the symmetry breaking parameters set at a high energy scale, and then use renormalisation group equations to arrive at the corresponding masses and couplings at lower energies. One particular example, which we will consider in this paper, is the CMSSM, where the model is defined by five free parameters:

$$m_0; m_{\frac{1}{2}}; A_0; \tan\beta; \text{sgn}\mu; \quad (1)$$

Here m_0 is the universal scalar mass, $m_{\frac{1}{2}}$ the gaugino mass parameter, A_0 the trilinear coupling between Higgs bosons, squarks and sleptons, $\tan\beta$ the ratio of vacuum expectation values of up-type and down-type Higgs bosons, and $\text{sgn}\mu$ the sign of the Higgs mixing parameter. The parameters m_0 , $m_{\frac{1}{2}}$ and A_0 are defined at the GUT scale (10^{16} GeV), whereas $\tan\beta$ and $\text{sgn}\mu$ are defined at the weak scale. Most authors define the CMSSM and mSUGRA (a ‘minimal SUPERGRAvity-inspired’ parametrisation of the MSSM) identically, and refer to them interchangeably; some other definitions of mSUGRA do exist, but the CMSSM is unambiguous.

In the literature, several regions have been identified where a neutralino LSP provides the right relic abundance of dark matter. These regions are then further constrained by accelerator searches. The regions that are still viable are the stau coannihilation region, where the stau is almost degenerate with the LSP (and the correct DM abundance is achieved by coannihilations), the focus point region (where the LSP is Higgsino-like), and the funnel regions, where LSP annihilation is increased by resonance interactions with MSSM Higgs particles.

4 Analysis

The flux delivered by annihilating DM can be calculated with [20]:

$$\begin{aligned} \Phi(E) &= 2.8 \cdot 10^{-12} \text{ cm}^{-2} \text{ s}^{-1} \text{ sr}^{-1} \cdot \frac{dN_\gamma}{dE} \frac{\langle\sigma v\rangle}{\text{pb} \cdot c} \left(\frac{1 \text{ TeV}}{m_\chi}\right)^2 \cdot \bar{J}(\Delta\Omega)\Delta\Omega \\ \Delta\Omega &= \frac{1}{8.5 \text{ kpc} \cdot (0.3 \text{ GeV cm}^{-3})^2} \int_{\Delta\Omega} d\Omega \int_{\text{los}} ds \varrho^2 \end{aligned} \quad (2)$$

where dN/dE describes the photon spectrum per annihilation, $\langle\sigma v\rangle$ is the thermally-averaged, velocity-weighted annihilation cross-section in the zero velocity limit (in the following simply denoted “cross section”), m_χ is the mass of the annihilating DM particle and ρ is its density, which is integrated along the line of sight (los) and over the observed solid angle of $\Delta\Omega = 1.16\cdot 10^{-5}$ sr for the GC, $\Delta\Omega = 2\cdot 10^{-5}$ sr for SgrD, and $\Delta\Omega = 10^{-5}$ sr for Carina and Sculptor. For the galactic halo the signal- and background regions are defined more complicated than for the other targets. The J -factor for this $\bar{J}(\Delta\Omega)$ represents the difference between the averaged line of sight integral in the signal and in the background region.

5 CMSSM random scan with data from the Galactic Centre

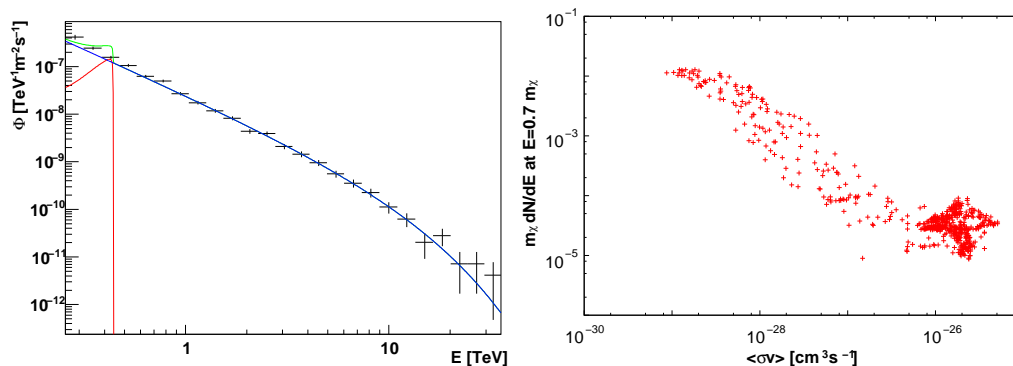


Figure 1: **Left:** Example of a comparison between data and model annihilation spectrum. The crosses show the measured spectrum published by the H.E.S.S. collaboration [4]. The red line shows Φ_{DM} the calculated dark matter spectrum for $m_0 = 438$ GeV, $m_{\frac{1}{2}} = 1030$ GeV, $A_0 = 0$, $\tan\beta = 39.1$, $\text{sgn}\mu = +1$ and $\bar{J}(\Delta\Omega)\Delta\Omega = 350$ sr (Moore profile). The blue line represents Φ_{bg} , the background model (a power law with exponential cutoff) that delivers the best fit as part of $\Phi_{\text{total}} = \Phi_{\text{DM}} + \Phi_{\text{bg}}$. **Right:** Correlation plot for the annihilation cross section $\langle\sigma v\rangle$ and γ -ray yield dN/dx with $x = E_\gamma/m_\chi$ at $x = 0.7$, showing the indicative number of photons per annihilation with energies just below the WIMP mass. Because IB has a harder gamma-ray spectrum than pion decay, for a fixed $\langle\sigma v\rangle$ models with larger yields at $E = 0.7m_\chi$ show stronger IB. Here we see that for the points that passed our relic density and accelerator cuts, the yield into photons with energies near the WIMP mass decreases as the cross-section increases, indicating that IB is much stronger in models with lower annihilation cross-sections.

Earlier analysis of the GC by H.E.S.S. showed that DM alone cannot be responsible for

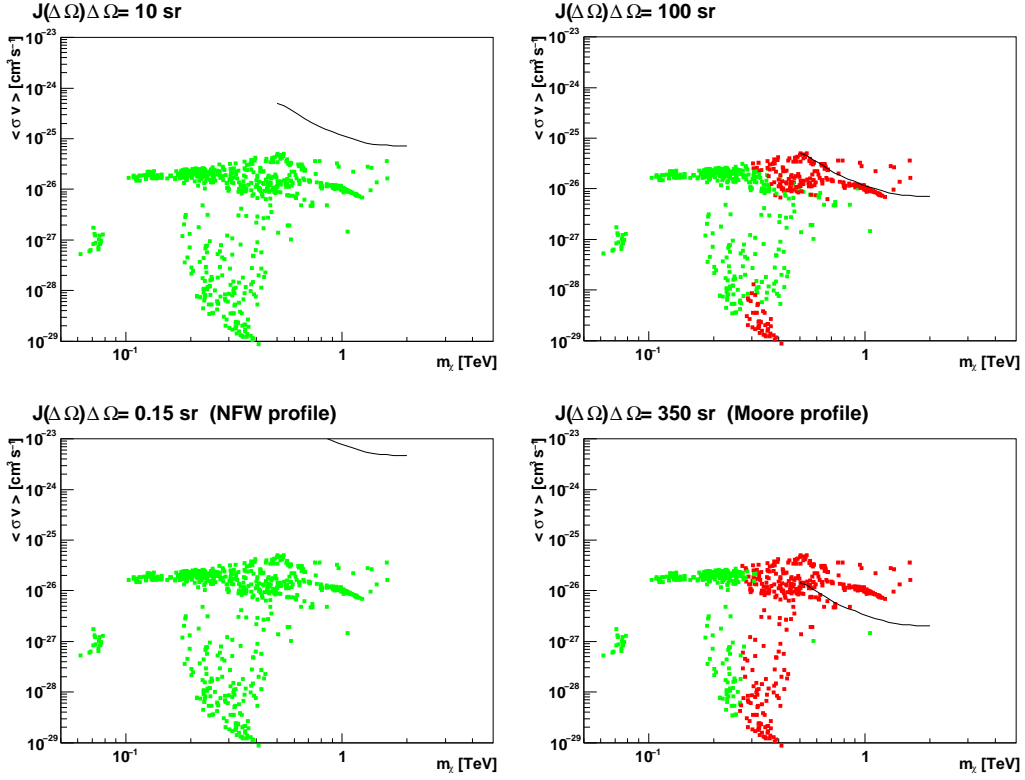


Figure 2: Rejection plots in the plane spanned by the neutralino mass m_χ and the annihilation cross section $\langle\sigma v\rangle$. The green points represent models consistent with the data, and red points models that are not consistent (at 90% CL). The black line shows the upper limit of $\langle\sigma v\rangle$ as function of m_χ , if annihilation of neutralinos proceeded entirely as $\chi\chi \rightarrow b\bar{b}$. In the top row, $\bar{J}(\Delta\Omega)\Delta\Omega$ increases from 10 sr (upper left) to 100 sr (upper right). The plots for an NFW profile ($\bar{J}(\Delta\Omega)\Delta\Omega = 0.15$ sr) and a Moore profile ($\bar{J}(\Delta\Omega)\Delta\Omega = 350$ sr) are shown in the lower row.

the observed spectrum [5]. We therefore consider an energy spectrum

$$\Phi_{\text{total}}(E) = \Phi_{\text{DM}}(E) + \Phi_{\text{bg}}(E), \quad (3)$$

composed of a DM component Φ_{DM} and an empirically-determined background, assumed to take the form of a power law with an exponential cut-off:

$$\Phi_{\text{bg}}(E) = \Phi_0 \cdot \left(\frac{E}{1 \text{ TeV}}\right)^{-\Gamma} \exp(-E/E_{\text{cut}}), \quad (4)$$

where Φ_0 is the flux normalisation, Γ represents the spectral slope and E_{cut} the cutoff energy. Such a form for the background provides quite a good fit to the observed spectrum

[5, 4], and is generally representative of typical astrophysical gamma-ray sources. In our scans, we fit Φ_0 , Γ and E_{cut} individually for each DM model in the CMSSM.

As a first check, we randomly chose 622 CMSSM models whose relic densities fit within the observed band ($0.094 \leq \Omega_{\text{DM}} h^2 \leq 0.129$) from 3 years WMAP observations [21], and pass similar accelerator bounds included in DarkSUSY 5.0.4. The CMSSM parameters in this scan lie in the following ranges: $10 \text{ GeV} \leq m_0 \leq 1000 \text{ GeV}$, $10 \text{ GeV} \leq m_{\frac{1}{2}} \leq 1000 \text{ GeV}$, $A_0 = 0$, $0 \leq \tan \beta \leq 60$, $\text{sgn} \mu \in \{-1, 1\}$. Whether a model (CMSSM parameters and chosen J factor) is compatible with the measured data is decided by a χ^2 -test. We fit $\Phi_{\text{total}}(E)$ to the data for each model, keeping the parameters for $\Phi_{\text{DM}}(E)$ fixed and the parameters for $\Phi_{\text{bg}}(E)$ free. An example of such a comparison is shown in the left panel of Figure 1.

A model (with an assumed value for $\bar{J}(\Delta\Omega)\Delta\Omega$) is defined as compatible with the data if the resulting $\chi^2 < 14.04$; the 90% threshold value of the χ^2 distribution with $N_{\text{bins}} - N_{\text{free}} = 25 - 3$ degrees of freedom. Results can be seen in Figure 2. Here we show whether a model – represented by a point in the m_χ - $\langle\sigma v\rangle$ -plane – is compatible with the measured spectrum or not, given different assumed values of $\bar{J}(\Delta\Omega)\Delta\Omega$. We also indicate the upper limit obtained if one assumes 100% annihilation into $b\bar{b}$, as has often been done in previous analysis. For comparison, the J factor for an NFW profile would be $\bar{J}(\Delta\Omega)\Delta\Omega|_{\text{NFW}} = 0.15 \text{ sr}$ and for a Moore profile $\bar{J}(\Delta\Omega)\Delta\Omega|_{\text{Moore}} = 350 \text{ sr}$.

For $\bar{J}(\Delta\Omega)\Delta\Omega \gtrsim 10 \text{ sr}$ the data begin to limit models from high cross-sections downward (into the focus point region). In addition, the parameter space is truncated from low cross-sections upward (into the coannihilation region) due to IB, as the number of photons from these processes and the annihilation cross-section are anti-correlated (see the right panel of Figure 1). For $\bar{J}(\Delta\Omega)\Delta\Omega \gtrsim 100$ the two limiting fronts meet. Models with $m_\chi \lesssim 200 \text{ GeV}$ remain allowed, because they do not affect the spectrum in the energy range observed by H.E.S.S.. A few models with $m_\chi \gtrsim 500 \text{ GeV} - 1000 \text{ GeV}$ and $\langle\sigma v\rangle \lesssim 10^{-27} \text{ cm}^{-3}\text{s}^{-1}$ also remain allowed.

A random scan is however not sufficient when dealing with a complicated parameter space with many dimensions, such as the CMSSM. Nuisance parameters that could substantially affect model predictions, such as the top quark mass, should be taken into account. Points should be measured against a whole range of observables, and given a properly-defined statistical likelihood rather than just ruled in or out. Sophisticated scanning algorithms should be used to make sure that all relevant parts of the parameter space have been probed, and in a way that allows valid statistical inference to be performed on the resultant points. For these reasons, we performed additional likelihood-based scans.

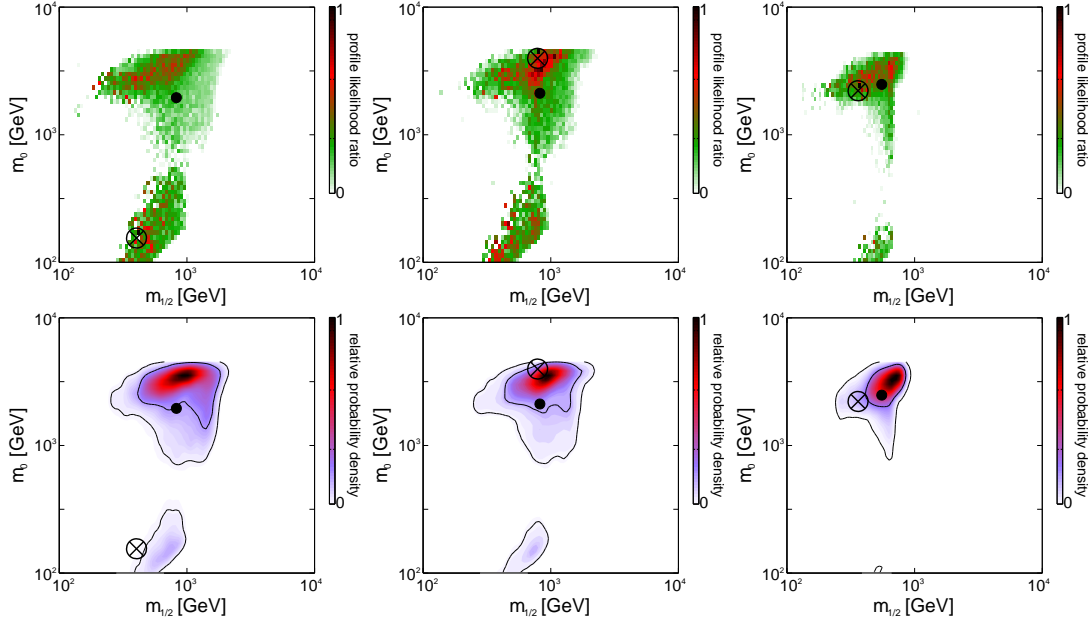


Figure 3: Profile likelihood ratios $\mathcal{L}/\mathcal{L}_{\text{best fit}}$ (upper row) and posterior probability density functions (lower row) normalized to the best fit point in the $m_{\frac{1}{2}}-m_0$ plane. In the left column H.E.S.S. data from the Galactic Centre have not been included in the scans. For the other plots, $\bar{J}(\Delta\Omega)\Delta\Omega = 10$ sr (middle) and 100 sr (right). The \otimes marks the best fit point, while the \bullet marks the centre of gravity of the distribution. Contours in the lower plots surround 68% and 95% credible regions.

6 CMSSM likelihood scan with data from the Galactic Centre

Our analysis is based on SuperBayeS, a package that scans the CMSSM parameter space and computes various observables, in particular the gamma-ray spectrum for a given CMSSM model, by interfacing with DarkSUSY. It performs statistical inference by comparing the computed values of the observables to experimental data, using a full likelihood construction. SuperBayeS also implements sophisticated scanning algorithms; in our scans, we chose the MultiNest [10] nested sampling algorithm, with 4000 live points. In each iteration step of this algorithm the point with the worst likelihood in a set of points in parameter space is replaced by a point with a better likelihood. In order to increase the possibility to find such a point, the border of the region surrounding all other points has to be described. This way this region nest the best fit points iteratively. We used the modified version of SuperBayeS 1.35 described in [2] for the analysis of H.E.S.S. data, supplemented

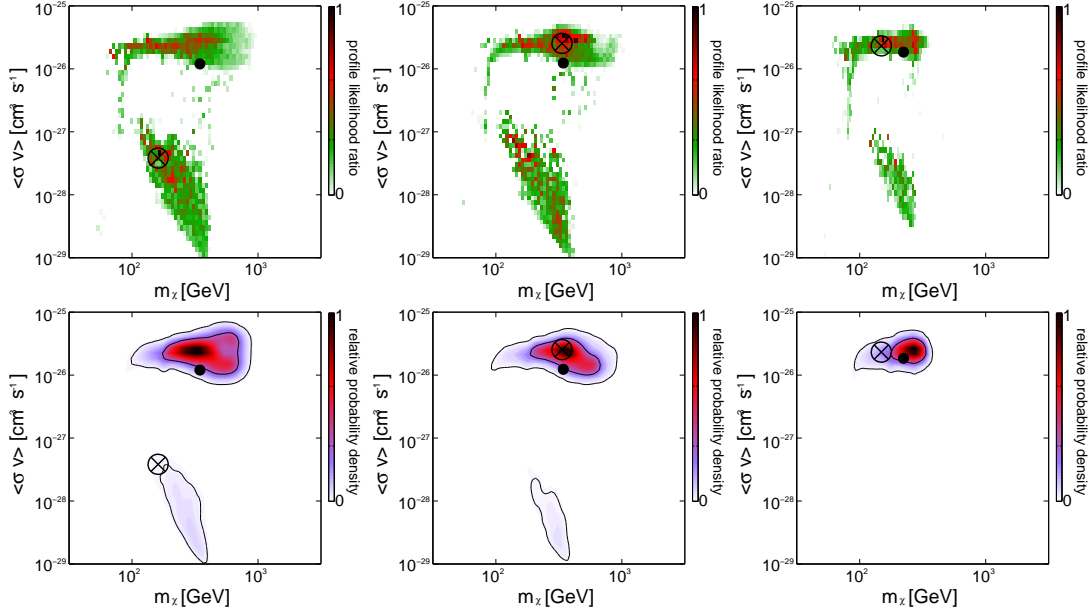


Figure 4: Profile likelihoods $\mathcal{L}/\mathcal{L}_{\text{best fit}}$ (upper row) and posterior probability density functions (lower row) normalized to the best fit point in the m_χ - $\langle\sigma v\rangle$ plane. In the left column H.E.S.S. data from the Galactic Centre have not been included in the scans. For the other plots, $\bar{J}(\Delta\Omega)\Delta\Omega = 10$ sr (middle) and 100 sr (right). The \otimes marks the best fit point, while the \bullet marks the centre of gravity of the distribution. Contours in the lower plots surround 68% and 95% credible regions.

with an appropriate H.E.S.S. likelihood term (given below). This modified version employs DarkSUSY 5.0.4 for the calculation of relic densities and gamma-ray spectra, including the full calculation of internal bremsstrahlung (both VIB and FSR) [1] crucial for our analysis.

We scanned over $60 \text{ GeV} \leq m_0 \leq 4000 \text{ GeV}$, $60 \text{ GeV} \leq m_{\frac{1}{2}} \leq 4000 \text{ GeV}$, $-7000 \leq A_0 \leq 7000$ and $2 \leq \tan\beta \leq 65$, setting $\mu > 0$ and applying linear priors to the other parameters. We also scanned over the top and bottom quark masses, and the strong and electromagnetic coupling constants, treating them as SM nuisance parameters. We incorporate the effects of the nuisance parameters in our analysis by either computing the profile likelihood (i.e. maximising the likelihood with respect to the nuisance parameters, at each point in the CMSSM parameter space), or by marginalising over them, integrating the posterior distribution at each point in the CMSSM parameter space over the nuisance space. Similarly, we choose to present distributions and likelihoods for subsets of CMSSM parameters by further profiling or marginalising over the remaining CMSSM parameters.

We use the unfolded (deconvolved; see [4]) H.E.S.S. spectrum to directly compare with

the theoretically predicted gamma-ray spectrum. We also use the observables, experimental likelihoods and SM nuisance likelihoods described in Ref. [15]; these are also the same as we employed in Refs. [22, 2]. In particular, we compared the relic density to data from the 5-year Wilkinson Microwave Anisotropy Probe (WMAP), which found $\Omega_{\text{DM}}h^2 = 0.1099 \pm 0.0062$ at the 1σ level [23]. Other observables were: LEP constraints on sparticle masses and the Higgs mass, measurements of the anomalous magnetic moment of the muon ($g - 2$), the mass difference $m_{\bar{B}_s} - m_{B_s}$, and the branching fractions of the rare processes $b \rightarrow s\gamma$, $\bar{B}_u \rightarrow \nu\tau^-$ and $\bar{B}_s \rightarrow \mu^+\mu^-$.

The likelihood of one CMSSM model is defined by

$$-\ln \mathcal{L} = \sum_i -\ln \mathcal{L}_i \quad (5)$$

where \mathcal{L}_i is the likelihood associated with each individual observable. For the H.E.S.S. spectrum from the GC, we used

$$-\ln \mathcal{L}_{\text{H.E.S.S., GC}} = \frac{\chi^2}{2} \quad (6)$$

with the χ^2 described in the previous subsection.

In Figures 3 and 4 we show both the profile likelihood and the posterior probability density function (assuming flat priors) for three different scans. The value of $\bar{J}(\Delta\Omega)\Delta\Omega$ increases left to right from 0 sr – no dark matter in the GC region, no H.E.S.S. data included in the scan – to 100 sr in the last column. Figure 3 shows the results of the scans projected down into the $m_{\frac{1}{2}}-m_0$ plane, while Figure 4 shows the resulting distributions in the $m_{\chi^-}(\sigma v)$ plane.

We see from Figures 3 and 4 that with increasing $\bar{J}(\Delta\Omega)\Delta\Omega$, the likelihoods of points in the coannihilation region and the higher-mass part of the focus point are reduced. This can also be seen in the movement of the best-fit point from the tip of the coannihilation region to a low-mass part of the focus point when GC data are introduced. In contrast, the posterior mean does not move substantially when GC data are included in fits, reflecting the fact that the focus point carries the majority of the posterior mass when linear priors are employed, and is left largely intact after the application of GC data.

However, the values we have used for $\bar{J}(\Delta\Omega)\Delta\Omega$ in these scans with GC data are unrealistically large. The GC source delivers a strong astrophysical background, hindering dark matter investigations. The scanning technique will be useful for future observations of the GC region however, especially with upcoming experiments like the Čerenkov Telescope Array (CTA).

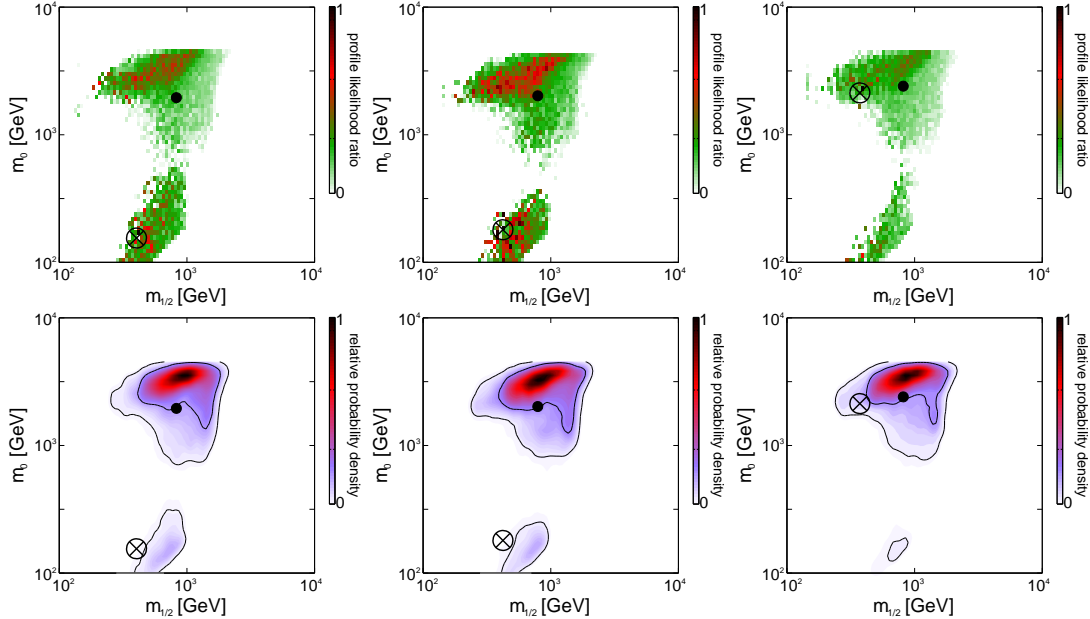


Figure 5: Profile likelihood ratios $\mathcal{L}/\mathcal{L}_{\text{best fit}}$ (upper row) and posterior probability density functions (lower row) normalized to the best fit point in the $m_{\frac{1}{2}}-m_0$ plane. In the left column H.E.S.S. data from the (SgrD) have not been included in the scans. For the other plots, we assume an NFW (middle) or a cored DM profile (right). The \otimes marks the best fit point, while the \bullet marks the centre of gravity of the distribution. The contours in the lower row plots surround the 68% and the 95% CL regions.

7 CMSSM likelihood scan with data from the Sagittarius dwarf galaxy

We assume two different DM profiles for the SgrD: a (cuspy) NFW and a cored profile. The first one delivers a scale factor of $\bar{J}(\Delta\Omega)\Delta\Omega|_{\text{NFW}} = 0.0186 \text{ sr}$, whereas the second one gives $\bar{J}(\Delta\Omega)\Delta\Omega|_{\text{cored}} = 0.636 \text{ sr}$ (with the definition in equation 4). Although it is less concentrated very close to the centre, the cored halo gives a larger J factor because its dark matter core radius is only 1.5 pc , which is within the observed solid angle. The small core radius leads to a steeper profile than NFW beyond $r = 1.5 \text{ pc}$, and a higher DM density around $r \sim 1.5 \text{ pc}$. The calculated upper limits just begin to touch interesting parts of parameter space (see the Erratum to [17]).

Because SgrD experiences heavy tidal disruptions, there are large uncertainties in its density profile, leading to a large uncertainty in the resultant J factor. We refer the reader to e.g. Refs. [17, 24] and references therein for more extensive discussions. Because

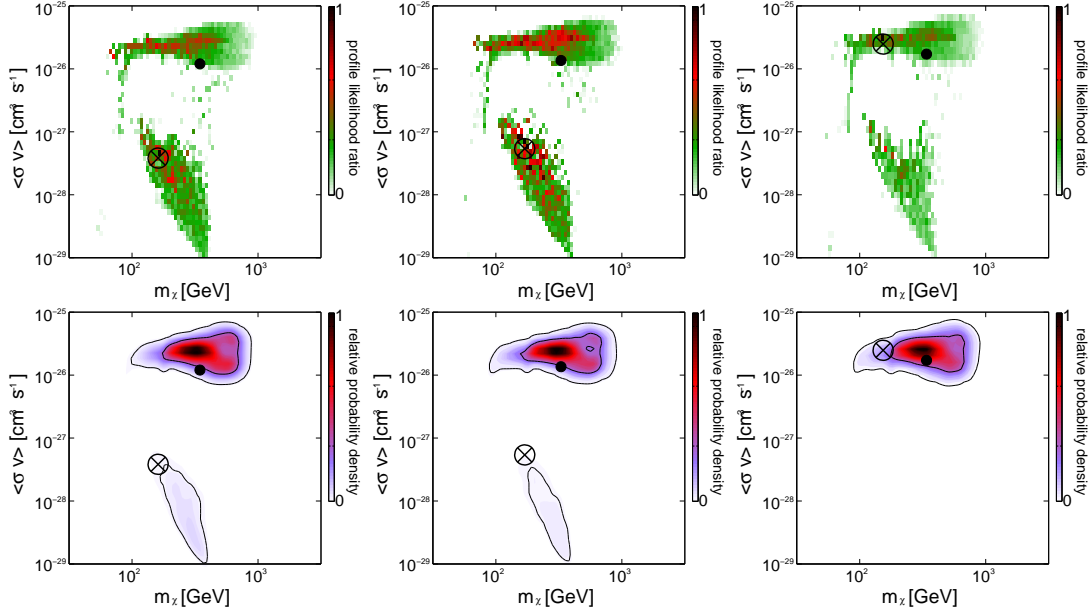


Figure 6: Profile likelihood ratios $\mathcal{L}/\mathcal{L}_{\text{best fit}}$ (upper row) and posterior probability density functions (lower row) normalized to the best fit point in the m_χ - $\langle\sigma v\rangle$ plane. In the left column H.E.S.S. data from the SgrD have not been included in the scans. For the other plots, we assume an NFW (middle) or a cored DM profile (right). The \otimes marks the best fit point, while the \bullet marks the center of gravity of the distribution. The contours in the lower row plots surround the 68% and the 95% CL regions.

of this uncertainty, in the following sections we also investigate the impacts of H.E.S.S. observations of the Galactic diffuse emission and other dwarf galaxies on the CMSSM, for which the J factors are better constrained.

In order to subtract the large cosmic ray background, this is estimated via a dedicated OFF-region in the H.E.S.S. analysis. This region might also contain a significant fraction of a hypothetical DM annihilation signal, which in this case would also be subtracted [25]. Since more than 90% of the DM signal of both the density profiles that we consider here originates from inside the ON-region (see [17]), this effect is negligible in our case.

To include these data into our likelihood calculation, we need an estimate of the flux and its error. 437 events were observed by H.E.S.S. in the “ON-region” centred on SgrD, and in the surrounding annular “OFF-region” 4270 events were collected. Since there is a difference of a factor of 10.1 in the areas of the sky covered by these two regions, there are 14.2 excess events observed in the ON-region. This is not statistically significant. Assuming that observed events follow Poisson statistics, the actual observed flux and its

error are $\Phi(E > 250 \text{ GeV}) = (0.9 \pm 1.4) \cdot 10^{-12} \text{ cm}^{-2} \text{ s}^{-1}$. We use this for the calculation of a (gaussian) likelihood.

Calculating the expected integrated flux from each CMSSM model and comparing with this value delivers us an easy estimate of the likelihood

$$-\ln \mathcal{L}_{\text{H.E.S.S., Sag}} = \frac{(\Phi_{\text{measured}} - \Phi_{\text{model}})^2}{2\sigma_{\Phi}^2} \quad (7)$$

The results of these scans (with somewhat more realistic density profiles than we employed for the GC) can be seen in Figures 5 and 6. We see that the coannihilation region becomes steadily more disfavoured for increasing J , due to the large virtual IB signal produced by models in this region. In general the only observable that strongly favours the coannihilation region over higher sparticle masses (as found in e.g. the focus point region) is $g - 2$, the anomalous magnetic moment of the muon [15]. When H.E.S.S. observations of the SgrD are included in the total likelihood, we see that their preference for the focus point over the stau coannihilation region essentially nullifies the impact of $g - 2$. This allows $b \rightarrow s\gamma$ to more clearly exert its preference for higher sparticle masses, leading to a stronger preference for focus point SUSY over the stau coannihilation region.

8 CMSSM likelihood scan with two other dwarf spheroidal galaxies

H.E.S.S. has observed the dwarf spheroidals Carina and Sculptor in 2008 and 2009 for 14.8 h and 11.8 h live time. No significant excess was detected [18]. We handle these two sources in the same way as the SgrD. The original H.E.S.S. paper gives event numbers, both in total and above some minimal energy E_{min} , the resulting upper limits on the number of excess events, and an integrated flux with $E > E_{\text{min}}$. In order to estimate the flux as we did with the SgrD, we used a simple toy Monte Carlo simulation to determine all combinations of event numbers with $E > E_{\text{min}}$ that reproduce the given upper limits on the excess of events. For our corresponding flux estimates, we then selected the largest event numbers that delivered the stated upper limits, as E_{min} is chosen very close to the energy threshold of the observations, so the majority of events should have $E > E_{\text{min}}$. Because in the majority of combinations the resulting estimated flux varies well within one standard deviation, the error we make with this method is small. The estimated fluxes are $\Phi(E > 320 \text{ GeV}) = (-1.99 \pm 1.88) \cdot 10^{-13} \text{ cm}^{-2} \text{ s}^{-1}$ for Carina and $\Phi(E > 220 \text{ GeV}) = (0.42 \pm 3.38) \cdot 10^{-13} \text{ cm}^{-2} \text{ s}^{-1}$ for Sculptor. The resulting implications for scans of the CMSSM parameter space can be seen in Figs. 7 and 8. In the centre panels of these figures, we see that the addition of Carina and Sculptor – with median values of the J factors reported in [18]: $\bar{J}(\Delta\Omega)\Delta\Omega|_{\text{Carina}} = 1.35 \cdot 10^{-4} \text{ sr}$ and $\bar{J}(\Delta\Omega)\Delta\Omega|_{\text{Sculptor}} = 1.91 \cdot 10^{-3} \text{ sr}$ – reduces the posterior probability of the stau coannihilation region relative to the focus point. This effect is not so dramatic as was seen with the cored-profile SgrD in the rightmost

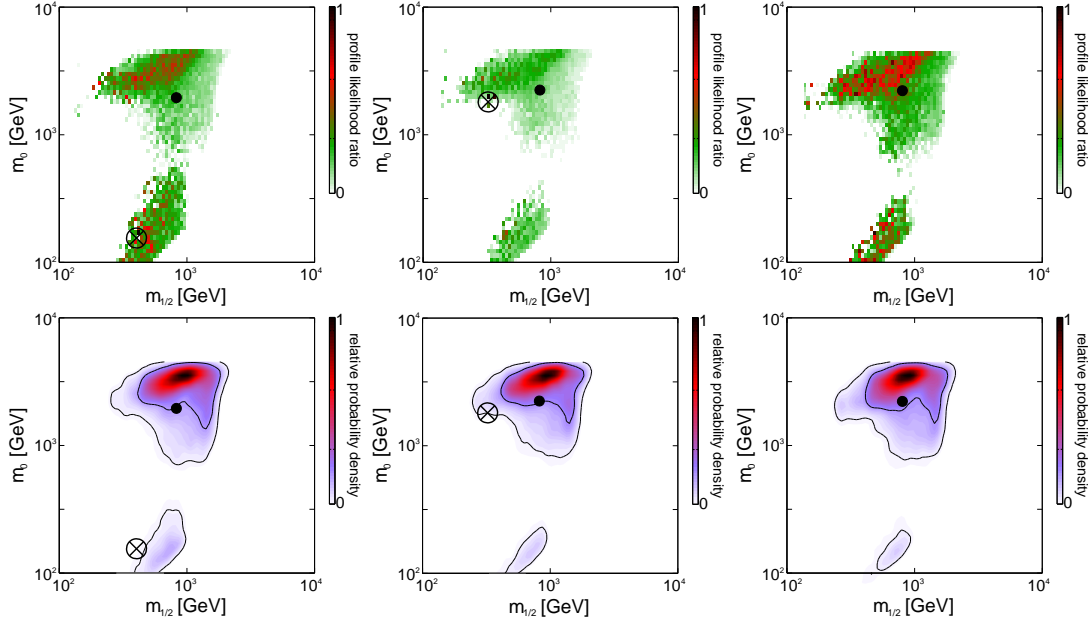


Figure 7: Profile likelihood ratios $\mathcal{L}/\mathcal{L}_{\text{best fit}}$ (upper row) and posterior probability density functions (lower row) normalized to the best fit point in the $m_{\frac{1}{2}}-m_0$ plane. In the left column no H.E.S.S. data are included in the scans. In the middle column Carina and Sculptor data are included. In the right column SgrD is also included.

panels of Figs. 5 and 6. In the rightmost panels of Figs. 7 and 8, we also show the impact of including all three dwarfs, this time with a SgrD J factor calculated as the mean of the J factors derived from NFW and cored profiles of $\bar{J}(\Delta\Omega)\Delta\Omega|_{\text{SgrD}} = 0.327$ sr. As expected, the coannihilation region is further disfavoured by the inclusion of the SgrD, though again not so severely as when this particular dwarf is employed with the (maximal) J factor corresponding to a cored density profile. Profile likelihoods follow essentially similar trends to posteriors, except for the fact that a highly isolated, very high likelihood best-fit point has been found in the scan including only Carina and Sculptor, but not in other scans. When the profile likelihood ratio is calculated using this best-fit value and plotted, the effect is to make all parts of the parameter space appear to have low likelihoods (i.e. essentially all of the allowed parameter space appears green in the middle panels of Figs. 7 and 8). This is easily understood as a result of the highly spiked nature of the CMSSM parameter space; here the scan has in fact managed to find its way part-way up the isolated focus point likelihood spike identified in [22]. This spike is typically missed in scans employing the standard configuration of the MultiNest algorithm (as we do here) [22, 26], as this mode is optimised more for mapping the posterior than producing fully-

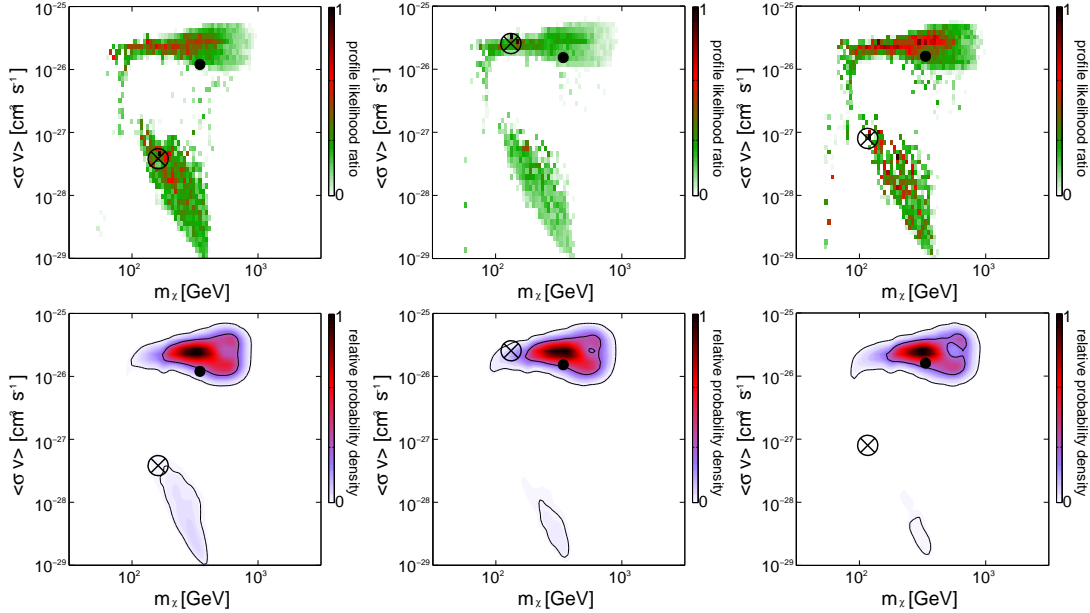


Figure 8: Profile likelihood ratios $\mathcal{L}/\mathcal{L}_{\text{best fit}}$ (upper row) and posterior probability density functions (lower row) normalized to the best fit point in the m_χ - $\langle\sigma v\rangle$ plane. In the left column no H.E.S.S. data are included in the scans. In the middle column Carina and Sculptor data are included. In the right column SgrD is also included.

converged profile likelihoods. Posteriors produced with these scanning parameters are of course fully converged; the profile likelihood results we present here should therefore be taken with something of a grain of salt, and the posteriors considered to be the primary result of this paper.

9 CMSSM likelihood scan with observations on the galactic halo

H.E.S.S. has performed observations near the galactic centre in the years from 2004 to 2008 in order to measure diffuse γ -radiation from the galactic halo. The residual spectrum does not show evidence of any excess γ -radiation [19]. This spectrum can be handled like the spectrum of the Galactic Centre, with the only difference being that the observable is intensity rather than flux. As in the previous section, we assume for the halo a median J factor between the minimum and maximum values given by [19] $\bar{J}(\Delta\Omega)|_{\text{halo}} = 1257$. For scans including the halo, we also included Carina and Sculptor (middle and rightmost panels of Figs. 9 and 10), as well as the SgrD (rightmost panels of Figs. 9 and 10). Comparing

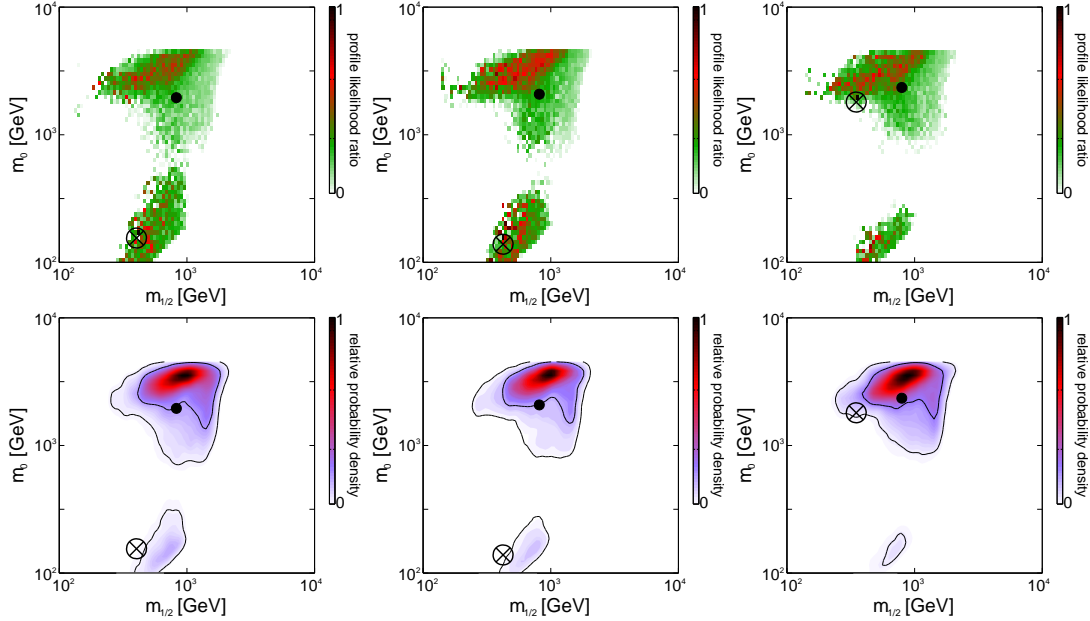


Figure 9: Profile likelihood ratios $\mathcal{L}/\mathcal{L}_{\text{best fit}}$ (upper row) and posterior probability density functions (lower row) normalized to the best fit point in the $m_{\frac{1}{2}}-m_0$ plane. In the left column no H.E.S.S. data are included in the scans. In the other two columns observations on the galactic halo are included, together with Carina and Sculptor (middle) and with Carina, Sculptor and the SgrD (right).

the middle panels of Figs. 9 and 10 to the middle panels of Figs. 7 and 8, we see that the addition of the Galactic halo data to scans including Carina and Sculptor in fact serves to *increase* the relative probability of the coannihilation region with respect to the focus point. This is because the halo constraint is rather weak, and serves only to directly constrain a few focus-point models with large cross-sections, slightly disfavouring the focus point in comparison to the coannihilation region, and therefore tempering the negative effect of the Carina and Sculptor dwarfs upon the relative probability of the coannihilation strip. When the SgrD is added (rightmost panels of Figs. 9 and 10), this effect is essentially swamped by the strong constraining effect of the SgrD data. This results in essentially the same level of preference for the focus point in scans including the SgrD with or without the halo data; differences between the rightmost panels of Figs. 9 and 10 and Figs. 7 and 8 is within the level of scanning noise.

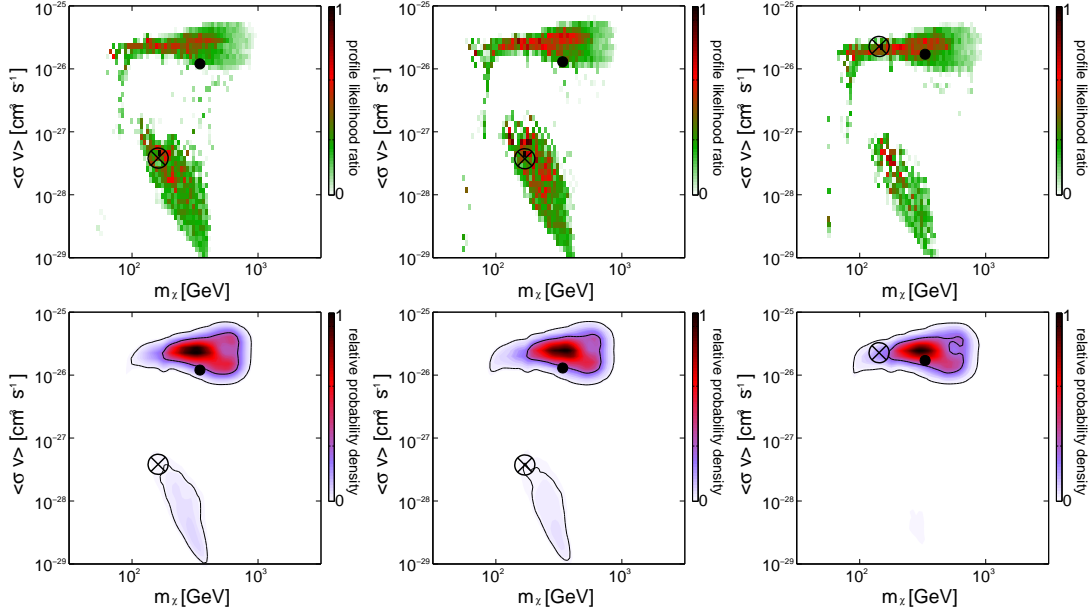


Figure 10: Profile likelihood ratios $\mathcal{L}/\mathcal{L}_{\text{best fit}}$ (upper row) and posterior probability density functions (lower row) normalized to the best fit point in the m_χ - $\langle\sigma v\rangle$ plane. In the left column no H.E.S.S. data are included in the scans. In the other two columns observations on the galactic halo are included, together with Carina and Sculptor (middle) and with Carina, Sculptor and the SgrD (right).

10 Summary, conclusions, and outlook

We have performed a scan over the CMSSM parameter space, taking into account a large range of experimental data at the composite likelihood level, and using nested sampling. We have done this in order to check what constraints are placed on CMSSM models by the combination of H.E.S.S. observations of dwarf spheroidal galaxies, the Galactic halo and the Galactic Centre.

Due to the strong astrophysical γ -ray source in or very near the GC, the search for DM there is strongly handicapped, so the data are not very constraining. With unrealistic assumptions about the DM density profile around the GC, we showed some example constraints on the coannihilation region and focus-point neutralinos with large masses. These examples show how the scanning technique will be useful for future observations with the next generation of γ -ray experiments, such as CTA.

For dwarf galaxies and the Galactic halo we also obtained constraints on the coannihilation region and high-mass parts of the focus point, even with realistic density profiles. These constraints result from the combination of the energy reach of H.E.S.S. and a full

treatment of IB. Our results give the tightest constraints to date upon the coannihilation region of the MSSM.

There are however still large uncertainties in the DM density profile of the SgrD, due to strong tidal forces [17, 24]. This is unfortunate, as the SgrD potentially provides the strongest constraint on CMSSM coannihilation models. Future scans and limits based on the SgrD should become more robust as they eventually come to include the the dark matter halo parameters as nuisances, and observational constraints upon those parameters improve. Ultimately however, we see that including observations of Carina and Sculptor along with those of the SgrD, and assuming median values of all J factors, results in almost as strong a constraint on the coannihilation region as taking just the SgrD on its own, and using a maximal J factor. This speaks strongly to the robustness of the results we have presented in this paper.

The recently presented results from LHC [27] are not directly comparable with our results, since constraints are presented for fixed $\tan\beta = 3$ and $A_0 = 0$, which is actually not part of the most favoured 68% region that we find. However, ATLAS constrains gaugino masses below about 310 GeV and scalar masses below about 740 GeV. Most of the favoured region that we find is at either larger gaugino or larger scalar masses. Thus, the present ATLAS constraint can be expected to have a minor effect on the results presented here, see e.g. [28] for a more detailed discussion.

11 Acknowledgments

We would like to thank Agnieszka Jacholkowski and Ullrich Schwanke for fruitful discussions. We are grateful to the Swedish Research Council (VR) for financial support. JR is grateful to the Knut and Alice Wallenberg Foundation for financial support. JC is a Royal Swedish Academy of Sciences Research Fellow supported by a grant from the Knut and Alice Wallenberg Foundation. PS is supported by the Lorne Trottier Chair in Astrophysics and an Institute for Particle Physics Theory Fellowship.

References

- [1] T. Bringmann, L. Bergström, J. Edsjö, *Journal of High Energy Physics*, 1, 49 (2008)
- [2] P. Scott, J. Conrad, J. Edsjö, L. Bergström, C. Farnier, Y. Akrami, *Journal of Cosmology and Astroparticle Physics*, 1, 31 (2010)
- [3] F. Aharonian et al., *Astronomy and Astrophysics*, 425, L13 (2004)
- [4] F. Aharonian et al., *Astronomy and Astrophysics*, 503, 817 (2009)
- [5] F. Aharonian et al., *Physical Review Letters*, 97, 221102 (2006)

- [6] J. Ripken, G. Heinzlmann, J.F. Glicenstein, Proceedings of 30th International Cosmic Ray Conference, 2, 791 (2008)
- [7] P. Gondolo, J. Edsjö, P. Ullio, L. Bergström, M. Schelke, E.A. Baltz, Journal of Cosmology and Astro-Particle Physics, 7, 8 (2004)
- [8] <http://www.darksusy.org/>
- [9] R. R. de Austri, R. Trotta, L. Roszkowski, Journal of High Energy Physics, 5, 2 (2006)
- [10] F. Feroz, M. P. Hobson Monthly Notices of the Royal Astronomical Society, 384, 449 (2008)
- [11] <http://www.superbayes.org/>
- [12] L. Roszkowski, R. R. de Austri, R. Trotta, Journal of High Energy Physics, 4, 84 (2007)
- [13] L. Roszkowski, R. R. de Austri, R. Trotta, Journal of High Energy Physics, 7, 75 (2007)
- [14] R. Trotta, R. R. de Austri, L. Roszkowski, New Astronomy Reviews, 51, 316 (2007)
- [15] R. Trotta, F. Feroz, M. P. Hobson, Journal of High Energy Physics, 12, 24 (2008)
- [16] F. Aharonian et al., Astronomy and Astrophysics, 457, 899 (2006)
- [17] F. Aharonian et al., Astroparticle Physics, 29, 55 (2008) Erratum: Astroparticle Physics, 33, 274 (2010)
- [18] A. Abramowski et al., Astroparticle physics, 34, 608 (2011)
- [19] A. Abramowski et al., Physical Review Letters, 106, 161301 (2011)
- [20] L. Bergström, P. Ullio, J. Buckley, Astroparticle Physics, 9, 137 (1998)
- [21] D. N. Spergel et al., The Astrophysical Journal Supplement Series, 170, 377 (2007)
- [22] Y. Akrami, P. Scott, J. Edsjö, J. Conrad, L. Bergström, Journal of High Energy Physics, 4, 57 (2010)
- [23] J. Dunkley et al., Astrophysical Journal Supplement, 180, 306 (2009)
- [24] A. Viana, C. M. Medina, J. Peñarrubia, P. Brun, J. F. Glicenstein, K. Kosack, E. Moulin, M. Naumann-Godo, B. Peyaud, arXiv:1103.2627 (2011)

- [25] G. D. Mack, T. D. Jaques, J. F. Beacom, N. F. Bell, H. Yuksel, Physical Review D, 78, 063542 (2008)
- [26] F. Feroz, K. Cranmer, M. Hobson, R. Ruiz de Austri, R. Trotta, JHEP, 06, 042 (2011)
- [27] G. Aad et al., Physical Review Letters 106, 131802 (2011)
- [28] G. Bertone, D. G. Cerdeno, M. Fornasa, R. R. de Austri, C. Strece, R. Trotta, arXiv:1107.1715

